Observational evidence of generation and propagation of barotropic Rossby waves induced by tropical instability waves in the Northeastern Pacific

Kang-Nyeong Lee[1], Chanhyung Jeon[2], YoungHo Seung[1], Hong-Ryeol Shin[3], Seung-Kyu Son[4], and Jae-Hun Park[1*]

[1]Department of Ocean Sciences, Inha University, Incheon 22212, South Korea.

[2] Department of Oceanography, Pusan National University, Busan 46241, South Korea.

[3]Department of Atmospheric Sciences, Kongju National University, Kongju 32588, South Korea.

[4]Deep-sea and Seabed Mineral Resources Research Center, Korea Institute of Ocean Science & Technology, Busan 49111, South Korea.

Corresponding author: Jae-Hun Park (jaehunpark@inha.ac.kr)

Key Points:

- In-situ near-bottom current velocity records are significantly coherent with satellite-measured SSH related to tropical instability waves.
- Variations with periods of 25−40 days near-bottom currents are caused by northward propagating TIW-induced barotropic Rossby waves.
- TIW-induced barotropic Rossby waves vary inter-annually with maxima during the La Niña periods.

Abstract

Tropical instability waves (TIWs) in the equatorial eastern Pacific (EEP) exhibit 25–40-day westward-propagating fluctuations with seasonal and inter-annual variations, which are stronger during the July−December and La Niña periods. They likely transfer their energy northward by forming barotropic Rossby waves (BTRWs). Long-term near-bottom current measurements at 10.5°N and 131.3°W during 2004–2013 revealed a spectral peak at 25–40 days, where significant coherences were found with satellite-measured sea surface height in a wide region of EEP with maxima around 5°N. Simulated deep currents from a data-assimilated ocean model agree with the observed near-bottom currents, and both currents vary seasonally and interannually, consistent with the typical characteristics of TIW. Further analyses using 25–40-day bandpass-filtered barotropic velocity data from the model revealed that they reasonably satisfied the theoretical dispersion relation of TIW-induced BTRW ($BTRW_{TIW}$). This study provides the first observational evidence showing $BTRW_{TIW}$ propagating northward above 10°N in the northeastern Pacific.

Plain Language Summary

Tropical instability waves (TIWs), which are located at the boundary between the warm pool and the cold tongue in the eastern Pacific, propagate westward with 25–40-day periods and vary seasonally and interannually; stronger during July-December and La Niña periods. Near-bottom velocity measured over a 10-year period at 10.5°N, 131.3°W just above the northern boundary of the waves fluctuates with 25–40-day periods, coinciding with that of sea surface height (SSH) in the equatorial eastern Pacific, especially around 5°N. We find that the wavelike pattern has wave crests oriented southeast-northwest from the model, and that this pattern appears across the study area and has characteristics consistent with TIWs including seasonal and interannual variations with the typical wavenumber and frequency. This pattern was verified to be a barotropic Rossby wave (BTRW) through model results analysis. Thus, TIWs induce BTRWs that transfer their energy to the abyssal ocean above 10°N in the northeastern Pacific. This study provides the first observational evidence that near-bottom currents vary with tropical instability waves.

1 Introduction

Tropical instability waves (TIWs), which have a cusp-like shape with repetitive high amplitudes near 5°N around the boundary of the cold tongue in the equatorial eastern Pacific Ocean (Legeckis, 1977; Legeckis et al., 1983), can be observed using satellite-measured sea surface temperature (SST) and sea surface height (SSH). They are typically observed to propagate westward along approximately 5°N with a wavelength of 1000 km and a period of 25 days (Tanaka & Hibiya, 2019). Multilevel numerical simulations predicted them to have a period of 33 days (Cox, 1980).

TIWs are known to be generated by barotropic and baroclinic instabilities. Tchilibou (2018) verified from an oceanic general circulation model that the former generate TIWs with periods of 20−25 days caused by meridional shear between the equatorial undercurrent and south equatorial current, while the latter induce 33-day period waves caused by the south equatorial current and north equatorial countercurrent system. The waves by both instabilities have been easily revealed from satellite measurements, although these properties are not always remarkable (Chelton et al., 2000; An, 2008; Shinoda et al., 2009). TIWs exhibit seasonal variations in the occurrence of intense growth from July to December, with more energetic activities during La Niña periods, linked to the strengthening of upwelling in response to strong trade winds in the equatorial eastern Pacific (Contreras, 2002; Warner & Moum, 2019).

Previous studies have focused mainly on the effects of TIWs near the equatorial ocean because it is known that the waves play an important role in regional ecosystems and the balance of heat associated with advection in the equatorial surface ocean (Willett et al., 2006; Moum et al., 2009). Tanaka and Hibiya (2019) showed that TIWs are generated from meridional potential vorticity gradient changes at 3.5°N, while Farrar (2011) identified that TIWs can affect their energy up to approximately 20°N. The longitude-time band-pass filtered SSH shows a structure of TIW at 0°−10°N and a propagation of barotropic Rossby waves (BTRWs) induced by TIW north of 10°N. Furthermore, using both results from barotropic ocean model and newly gridded satellite-measured SSH with a mapping algorithm without latitudinal variation in its filtering properties, Farrar et al. (2021) showed that the propagation of the BTRWs continues until 35°N. However, these studies lacked in-situ observations.

Here, we used 10-year-long in-situ near-bottom current measurements which were recorded at a site located north away from active region of TIW. The in-situ near-bottom current measurements clearly show that the TIW-induced BTRWs propagate northward. The processes of energy propagation in the form of BTRWs were also analyzed through the satellite-measured SSH as well as the results of data-assimilated numerical simulation (GLORYS12V1). In addition, the long-term in-situ measurements, satellite measurements, and results of GLORYS12V1 between 2004 and 2013 enable the verification of interannual variations according to the El Niño-Southern Oscillation (ENSO).

2 Data and Methods

2.1 In-situ and satellite measurements and GLORYS12V1 model results

Long-term, half-hour interval near-bottom current data (U_{obs}, V_{obs}) were recorded at a depth of ~5000 m in the northeastern Pacific (10.5°N, 131.3°W; black star in Figure 1a) from August 21, 2004, to July 27, 2013. The observations were conducted as part of the Korea Deep Ocean Study (KODOS). To conduct the spectral analysis and squared-coherency analysis between in-situ data and other daily data explained below, the former were averaged over a day.

The analysis uses daily SSH data and 1/4° resolution absolute dynamic topography product from the Copernicus Climate Change Service (C3S) (SEALEVEL_GLO_PHY_CLIMATE_L4_REP_OBSERVATION_008_057). The SSH maps were produced by using sea-level data collected from two altimeters with orbits similar to the Topex/Poseidon and ERS-1 historical orbits, which are used to monitor the long-term evolution of SSH. The domain used was 0°–20°N and 140°–80°W during the same period of near-bottom current measurements.

We also used the results of a data-assimilated global ocean reanalysis numerical simulation (GLORYS12V1) to investigate the characteristics of TIW-induced BTRWs. The GLORYS12V1 product is provided by the Copernicus Marine Environment Monitoring Service (CMEMS), and its component is the Nucleus for a European Model of the Ocean (NEMO) platform. The daily mean GLORYS12V1 outputs have a spatial resolution of 1/12° × 1/12°. The selected domain for the analyses is the same as that of satellite measured SSH, but the data cover the period from January 1, 2004, to December 31, 2013.

2.2 Pre-processing of squared coherency

The squared coherency (hereafter referred to as coherence) between satellite-measured SSH and the time series of in-situ near-bottom current measurements was performed as follows. The former data, a function of longitude, latitude, and time, were bandpass filtered only for longitudinal band with pass-band wavelengths 9°–20° in longitude depending on the latitudes considered. In longitudinal filtering, the typical zonal wavelengths of the TIW are taken into account. Spectral analysis was applied to 3263 days-long time series. A hamming window of length 512 days was used on the segment, and a 50% overlap was used to increase the number of segments. The 95% significance level, determined by the number of segments and the window, is 0.18 (Thomson & Emery, 2014).

2.3 Complex empirical orthogonal function analysis

The Complex empirical orthogonal function (CEOF) analysis (Hernández-Guerra & Nykjaer, 1997) using the barotropic velocity results, calculated from the depth average of the numerical simulation, requires a preprocessing procedure. The results of the numerical simulation were filtered using a longitude-latitude-time band-pass filter (zonal wavelengths of 9°−20° in longitude, meridional wavelengths of 9°–20° in latitude, and periods of 25–40 days). Processing using the longitudinal band-pass filter was the same as that of the satellite-measured SSH, but the latitudinal band-pass filter has a constant cut-off length for all longitudes. These filtering steps were performed sequentially, first for longitude, next for latitude, and lastly for time. The three dimensions (longitude-latitude-time) filtered data were converted to two dimensions (spatio-temporal section) and the two components were concatenated along the row to consider a spatial relationship between them. The results of CEOF analyses are shown separately for zonal (U_{bt}) and meridional (V_{bt}) components.

3 Results

To compare the satellite-measured SSH and in-situ near-bottom current velocity (U_{obs},V_{obs}) with each other, two time series of SSH located at different latitudes, indicated by black and red stars in Figure 1a, were used. One is located at the mooring observation site (SSH_{high}), and the other is located at 5°N, 131.3°W (SSH_{low}). Figure 1b shows the time series of satellite-measured SSH_{low}, SSH_{high}, and in-situ near-bottom current velocity (U_{obs}, V_{obs}) that were filtered by using a band-pass filter with cutoff periods of 25−40 days. Gray lines superimposed on the filtered data show the original time series. The time series corresponding to red star are surrounded by a box with red dashed lines, and those to black star are surrounded by a box with black dashed lines. Maximum speed of the original (filtered) U_{obs} and V_{obs} are 13.5 (2.8) cm/s and 16.7 (3.5) cm/s. The filtered time series of U_{obs} and V_{obs} exhibit similar variations to SSH_{low} with about a month period, which is consistent with the temporal variation of TIWs reported by Lyman et al., (2007). They are strengthened during the late summer and early winter months, with inter-annual variations. In contrast, the SSH_{high} shows no resemblance to others and has substantially smaller values than the original time series. The results of spectral analysis also show the same tendency. The spectral peak around the period of 32 days clearly shows that the filtered time series has the similar periodicity to the TIW (top panels in Figure 1c). In contrast, the power spectral density (PSD) of the SSH_{high} does not show any significant peaks around that period (gray line in Figure 1c).

Coherences between the SSH_{low} and the U_{obs} (between the SSH_{low} and the V_{obs}) exhibit high values (> 0.55) around the period of 32 days with a maximum value at the period of 32 days (at the period of 28 days) (middle panel in Figure 1c). The SSH_{low} leads the U_{obs} (the V_{obs} leads the SSH_{low}) by 115° at the period of 32 days (-56° at the period of 28 days). On the other hand, coherences between the SSH_{high} and either the U_{obs} or the V_{obs} appear to be much smaller, although they exceed the significance level 0.18 around the period of 32 days. These results suggest that the high coherence (> 0.8) between the SSH_{low} and U_{obs} around the period of 32 days should be associated with the TIW-related processes in the equatorial eastern Pacific.

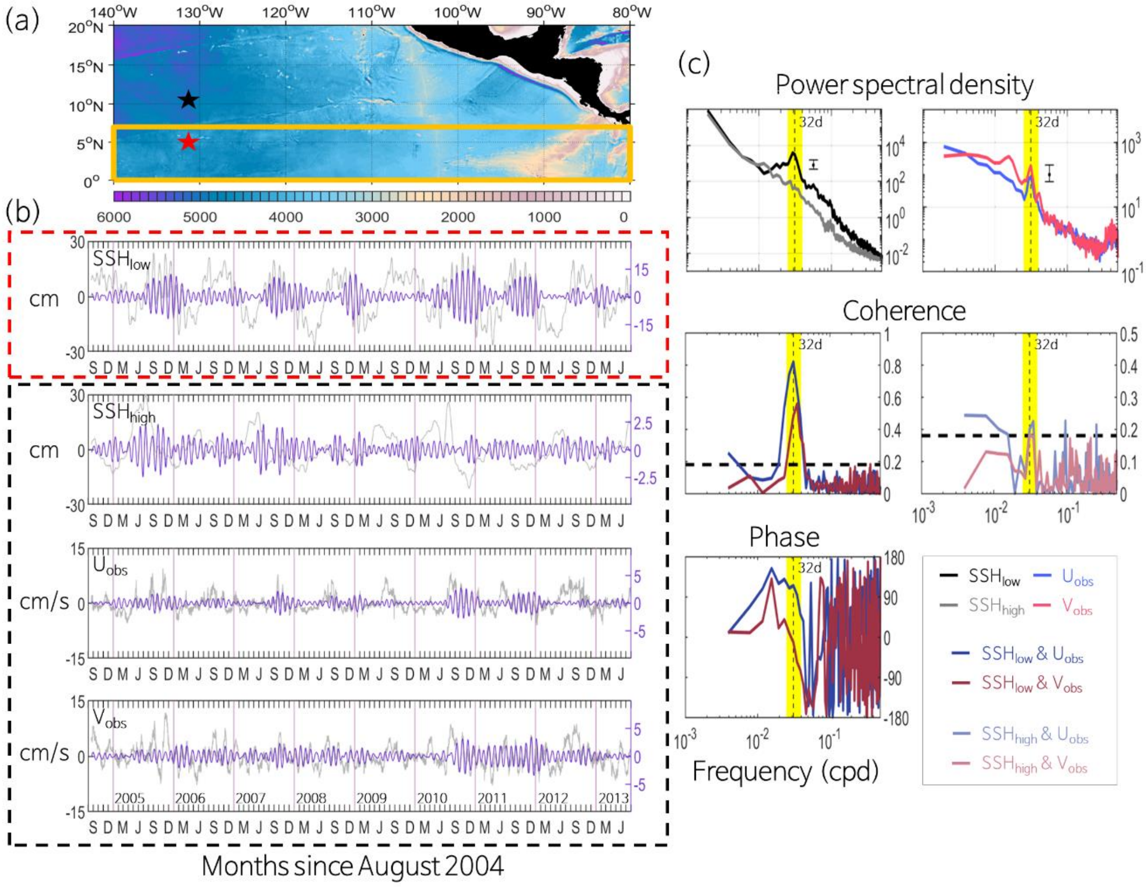

Figure 1. (a) Bathymetry of numerical model (GLORYS12V1) domain, with black and red stars indicating, respectively, the location of the mooring observation site (10.5°N, 131.3°W) and SSH_{low} (5°N, 131.3°W). (b) Bandpass filtered time series (purple lines) of SSH_{low}, SSH_{high}, U_{obs}, and V_{obs}, having periods of 25–40 days superimposed on their original time series (light gray lines). Note that the color of time series matches with that of the axis of ordinates. (c) Power spectral density of SSH_{low} (black line), SSH_{high} (gray line), U_{obs} (blue line), and V_{obs} (pink line). Vertical bars indicate the 95% confidence interval. Coherences and phases between SSH_{low} and U_{obs} (SSH_{low} and V_{obs}), and SSH_{high} and U_{obs} (SSH_{high} and V_{obs}) are represented by a dark blue line (dark pink line), and a light blue line (light pink line), respectively. The phases between the SSH_{high} and the in-situ near-bottom current data are not shown here because of the low coherences between them. Horizontal dashed lines denote the 95% significance level. Vertical dashed lines indicate 32-day periods and yellow shaded areas indicate a TIW frequency band (periods of 25–40 days).

The zonal wavenumber-frequency power spectral density (two-dimensional PSD) averaged over 0°–7°N for satellite-measured SSH resembles the spectrum shown in Farrar (2011), which is thought to be a common feature associated with the TIW (Figure 2a). The domain used was 0°–7°N, 140°–80°W (yellow box in Figure 1a) and the observation period is from January 1, 2004 to December 31, 2013. Two-dimensional PSDs from longitude-time sections of the data at different latitudes are averaged, resulting in a function of negative zonal wavenumber and frequency. For convenience, the wavenumber is expressed in wave length on the horizontal axis (Figure 2). The resulting two-dimensional PSD may allow us to identify the spatio-temporal character of the observed features in the area of active TIWs (the regions surrounded by a yellow box in Figure 1a). Two-dimensional PSDs of the numerical simulation results show high values in the frequency band of periods 25–40 days and in the wavenumber band of wavelength 1000–2300 km with concentrated values near the period of 33 days (the domains surrounded by the boxes with white lines in Figures 2b–d). It is suggested that TIWs can affect the currents in the deep layer because the distributions of energy density from the numerical simulation shows similar characters to those of TIWs.

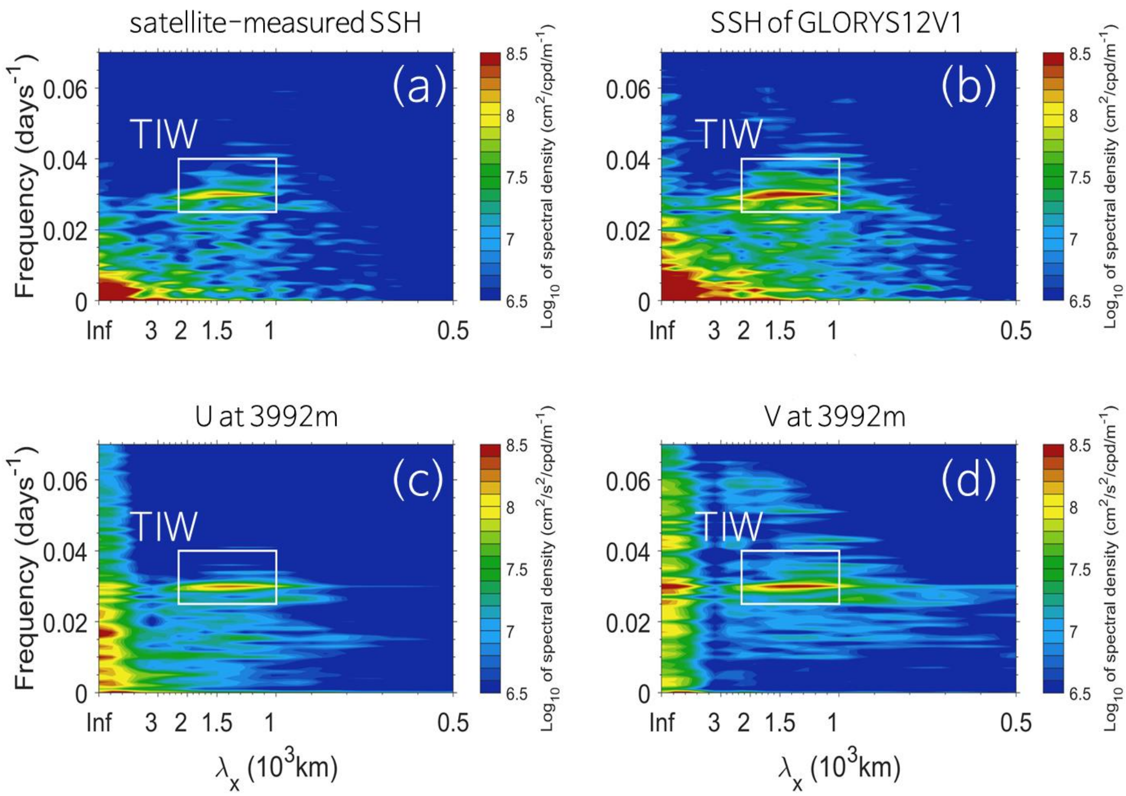

Figure 2. Zonal wavenumber-frequency power spectral density (PSD) averaged over 0° −7°N for (a) satellite-measured SSH, and numerically simulated (b) SSH and (c, d) velocity components at 3992-m depth from GLORYS12V1. Horizontal axis is zonal wavenumber expressed in wavelength in km referred to 3.5°N. White box is the range of frequency and wavenumber for the typical TIWs which has periods of 25–40 days and zonal wavelengths of 1000–2300 km.

To extend the coherence analysis shown in Figure 1c, we calculated the coherences and phases between gridded satellite-measured SSH and in-situ near-bottom velocity components (U_{obs}, V_{obs}), and mapped them by averaging over the frequency range of periods 25–40 days (Figures 3a–d). The coherence map between the SSH and U_{obs} (V_{obs}) exhibits high values larger than 0.6 (0.5) especially south (southwest) of the mooring observation site. These high coherences strongly suggest that both the SSH and the observed near-bottom current are related with the TIW.

The positive phase relationship in the region of high coherence (> 0.6) between SSH and U_{obs} suggests that the SSH which reflects the TIWs in this region leads U_{obs}. In contrast, the negative phase relationship in the same region between SSH and V_{obs} suggests that V_{obs}

leads the SSH. These results about the phase relationship strongly indicate a southwestward phase propagation at periods 25–40 days. There is an abrupt change in phase across the latitude 10°N consistently with the cross-spectral phase estimated in the previous study where satellite-measured gridded SSH data relative to 5°N are used (Farrar, 2011). This abrupt change indicates that the variation of our filtered in-situ near-bottom velocity is caused by TIW-induced BTRWs, as suggested by Farrar (2011), rather than TIWs itself. The phase propagation of the BTRW is more clearly seen in the numerically simulated velocity field as follows.

The four maps in Figures 3e–h exhibit the first-mode CEOF phase and amplitude of the filtered barotropic velocity fields (U_{bt}, V_{bt}) obtained the numerical simulation. The phase progresses southwestward similar to that at latitudes higher than 10°N, as shown in Figures 3c and 3d. The amplitude maps show high values in the west of 115°W with slightly low values along equator and 7°N in Figure 3g (along 4°N in Figure 3h).

Linear theory predicts that southward propagating BTRW has a north component of group velocity which is proportional to $\overline{\eta v_a}$, where η is sea surface elevation, v_a is ageostrophic part of north component of current velocity and overbar denotes wave average (e.g., Gill 1982, p502). This can also be observationally supported by showing that $\overline{\eta v_a}$ obtained at the mooring observation site is indeed significantly positive. In doing this, two points should be noted. First, since $\overline{\eta v_g}$, with v_g the geostrophic part, vanishes, $\overline{\eta v_a}$ is replaced by $\overline{\eta (v_g + v_a)} = \overline{\eta v}$. Second, since the wave periods are variable (25–40 days), the wave average is replaced by the average over all observation period. As already suggested by the significance of coherence between η and v at the mooring observation site (Figure 1c and Figure 3b), the calculated $\overline{\eta v}$ is found to be 0.0031 $m^2\ s^{-1}$, higher than the 95% significance level of 0.0018 $m^2\ s^{-1}$. It can be said that the energy propagation of the BTRW of periods 25–40 days is significantly northward, away from the region of TIW, at the mooring observation site although the rate of propagation may not be high.

TIWs are known to strengthen during the La Niña period when the sea surface temperature is lower and sea surface pressure is higher than in normal years in the equatorial eastern Pacific (Wang & Fiedler, 2006). Time series of the amplitude of principal component of the first CEOF mode for the filtered barotropic velocity exhibits an inter-annual variation similar to that of the TIWs (Figure 3i). Large amplitudes are seen around La Niña periods (blue shades in Figure 3i). The largest amplitude occurs during the most intense La Niña periods (2007 and 2010). Thus, we can conclude that deep currents associated with TIW-induced BTRWs undergo an inter-annual variations at higher latitudes.

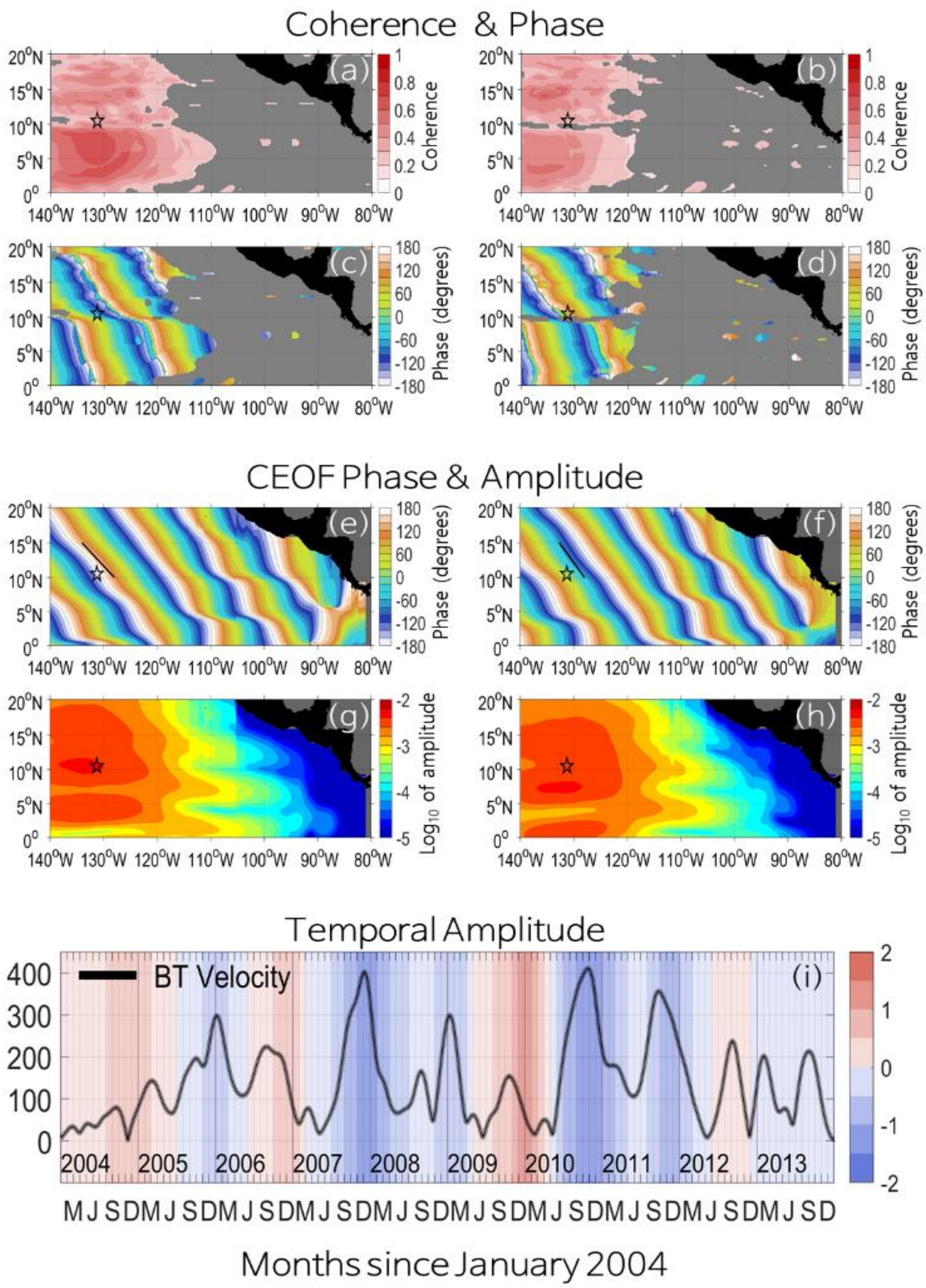

Figure 3. **(a, b)** Coherence and **(c, d)** phase maps between gridded satellite-measured SSH and observed near-bottom velocity components (U_{obs} and V_{obs}). **(a, b, c, d)** Left is for SSH and U_{obs}, and the right is for SSH and V_{obs}. The region with coherences under 95% significance level is gray-colored. **(e, f, g, h)** The first CEOF mode of the spatio-temporal band-pass filtered barotropic velocity components (U_{bt}, V_{bt}) obtained from the numerical simulation (GLORYS12V1) during 10 years from 2004 to 2013. Percentage of first CEOF mode is 56.5 %. Left is for U_{bt} and right is for V_{bt}. Upper is phase and lower is amplitude. **(e, f)** Superimposed black lines are co-phase line calculated from the CEOF phase. Black stars denote the location of mooring observation site. **(i)** Time series of the amplitude of principal component of the first CEOF mode for barotropic current velocity obtained from GLORYS12V1. Niño 3.4 indices (https://climatedataguide.ucar.edu/climate-data/nino-sst-indices-nino-12-3-34-4-oni-and-tni) based on a 30-year data are shown by using background

colors. Red denotes El Niño and blue denotes La Niña periods, respectively.

4 Discussions

The main result of the coherence analysis is that the in-situ near-bottom current velocity over the 10-year study period is significantly coherent with SSH at periods of 25−40 days at lower latitudes where energetic TIWs prevail, more than at the mooring site. The discontinuity along 10°N of the phase supports the fact that TIWs, which affect our near-bottom velocity observation, propagate northward with different phases across 10°N. This is consistent with the findings of Farrar (2011), who showed trapped baroclinic TIWs between the equator and 10°N superimposed on TIW-induced BTRWs with northward energy propagation.

To verify that the CEOF phase of the filtered barotropic velocity is associated with TIW-induced BTRW, we compare the wavenumbers calculated from the CEOF phases to the wavenumbers obtained theoretically using the dispersion relation of BTRW:

$$\omega = \frac{-\beta k}{k^2 + l^2} \qquad (1),$$

where ω is frequency, k and l are the zonal and meridional wavenumbers, respectively. β is the gradient of the Coriolis parameter at specific latitudes, and we take β at 10.5°N to be 2.25 × 10^{-11} m^{-1} s^{-1}. Note that, in Eq. (1), the Rossby radius is assumed to be much larger than the wavelength. The comparison was performed under the assumption that the TIW and TIW-induced BTRW have the same frequency and zonal wavenumber (Farrar, 2011).

The frequencies and zonal wavenumbers of TIW were estimated to be 1.8×10^{-6} s^{-1} < ω < 2.9×10^{-6} s^{-1} (periods of 25−40 days) and -6.4×10^{-6} m^{-1} < k < -2.9×10^{-6} m^{-1} (zonal wavelengths of 9°–20° of longitude) based on the two-dimensional PSDs of satellite-measured SSH (see Figure 2a). The meridional wavenumbers of BTRW were calculated by substituting the frequencies and zonal wavenumbers of TIW into Eq. (1). The theoretically possible range of frequencies and wavenumbers of TIW-induced BTRW appears in the wavenumber space to be the purple region in Figure 4. On the other hand, zonal and meridional wavenumbers are also calculated using the first-mode CEOF phases as follows. The zonal wavenumbers of U_{bt} and V_{bt} by using phases at two points (10.5°N, 126.3°W and 10.5°N, 136.3°W) are estimated to be -4.18×10^{-6} m^{-1} and -4.31×10^{-6} m^{-1} and the meridional wavenumbers of U_{bt} and V_{bt} by using phases at the two points (15.5°N, 131.3°W and 5.5°N, 131.3°W) are estimated to be -5.06×10^{-6} m^{-1} and -4.03×10^{-6} m^{-1}. Note that the co-phase line is shown as the black lines in the CEOF phase maps (Figures 3e and 3f). The estimated wavenumbers based on U_{bt} and V_{bt}, are marked by blue and pink small circles in the wavenumber space (Figure 4). It is quite encouraging that they fall within the possible range of frequency and wavenumber estimated earlier, supporting the fact that the first CEOF mode is quite compatible with the TIW-induced BTRW. The direction of group velocity corresponding to the estimated possible wave frequencies and wavenumbers is northward (Figure 4), as is deduced already from the measured near-bottom current and SSH_{high} data, $\overline{\eta v}$, at the mooring site.

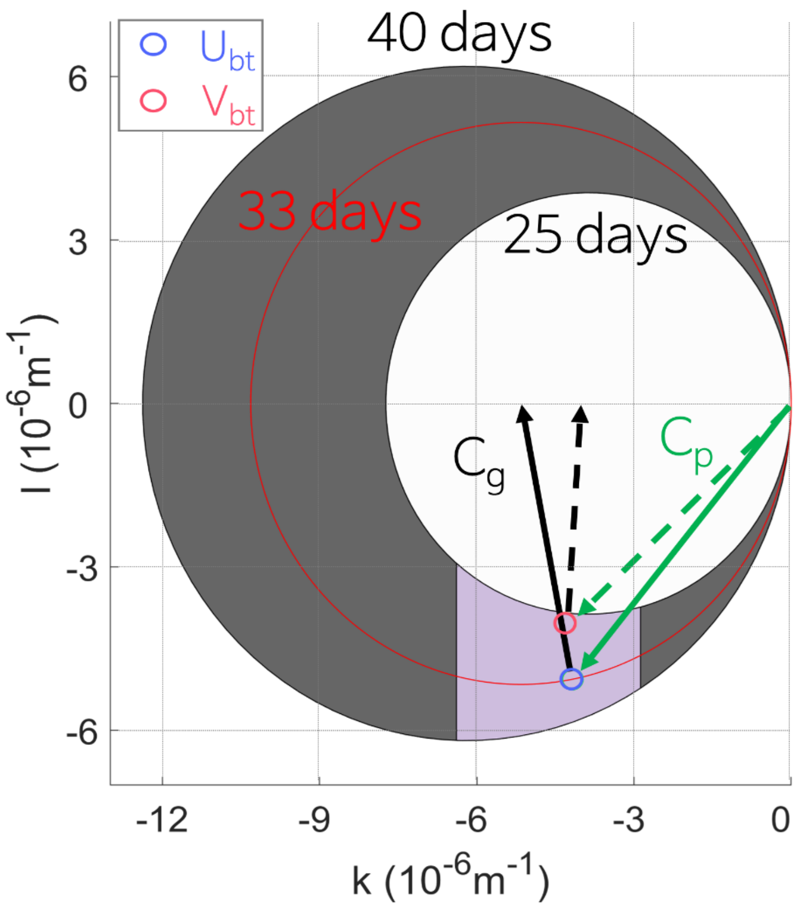

Figure 4. Dispersion relation curves of BTRW with periods of 25-40 days. The purple shading indicates theoretically possible ranges of frequency and wavenumber for TIW-induced BTRW. Large red circle corresponds to 33-day period BTRWs. Blue and pink small circles are wavenumbers estimated from numerical results U_{bt} and V_{bt}. Green and black solid (dashed) arrows are, respectively, phase and group velocities of TIW-induced BTRW obtained from U_{bt} (V_{bt}).

5 Conclusion

This study is the first to use long-term in-situ near-bottom current measurements to confirm that the TIW-induced BTRWs propagate their energy northward above 10°N in the northeastern Pacific Ocean. The filtered time series of in-situ near-bottom current velocity shows that the TIW-induced BTRWs induce a maximum velocity of approximately 3 cm/s at the near bottom and have variations similar to those of TIWs. It has been also evidenced from numerical simulation that this energy propagation was caused by the BTRWs, which showed inter-annual variations because the waves were derived from TIWs.

Our observation provides clear evidence that TIW-induced BTRWs transported the energy of the equatorial eastern Pacific Ocean to the abyssal ocean in high latitudes. The effects of TIWs transported to the abyssal ocean in a low energy environment, due to the lesser vertical gradient of density and variation of current, can lead to turbulence (Aleynik et al., 2017). The response of the bottom current is meaningful in that it is possible to affect the advection of abyssal resources, because the mooring observation site is located in the Clarion-Clippertone zone. Thus, the long-term in-situ near-bottom current velocity is also expected to improve the understanding of the distributions of mineral deposits and be used as an evaluation element in terms of abyssal mining.

Acknowledgments

This study is funded by “The study for the cooperative use of the research vessel” funded by Korea Institute of Ocean Science and Technology (KIOST) and the Ministry of Oceans and Fisheries of Korea (19992001).

Open Research

The filtered near-bottom current velocity data used in figures can be downloaded https://github.com/KNLeeinha/KOMO_CM.git and will be deposited Zenodo permanently if the manuscript is accepted. Absolute dynamic topography product was provided by the C3S, from their web site at https://doi.org/10.48670/moi-00145. GLORYS12V1 reanalysis data were provided by the CMEMS, from their web site at https://doi.org/10.48670/moi-00021.

References

Aleynik, D., Inall, M. E., Dale, A., & Vink, A. (2017). Impact of remotely generated eddies on plume dispersion at abyssal mining sites in the pacific. *Scientific Reports*, 7(16959), 1−14. https://doi.org/10.1038/s41598-017-16912-2

An, S.-I. (2008). Interannual variation of the tropical ocean instability wave and ENSO. *Journal of Climate*, 21(15), 3680−3686. https://doi.org/10.1175/2008JCLI1701.1

Chelton, D. B., Wentz, F. J., Gentemann, C. L., de Szoeke, R. A., & Schlax, M. G. (2000). Satellite microwave SST observations of transequatorial tropical instability waves. *Geophysical Research Letters*, 27(9), 1239−1242. https://doi.org/10.1029/1999GL011047

Contreras, R. F. (2002). Long-term observations of tropical instability waves. *Journal of Physical Oceanography*, 32(9), 2715−2722. https://doi.org/10.1175/1520-0485(2002)032<2715:LTOOTI>2.0.CO;2

Cox, M. D. (1980). Generation and propagation of 30-day waves in a numerical model of the pacific. *Journal of Physical Oceanography*, 10(8), 1168−1186. https://doi.org/10.1175/1520-0485(1980)010<1168:GAPODW>2.0.CO;2

Farrar, J. T. (2011). Barotropic Rossby waves radiating from tropical instability waves in the pacific ocean. *Journal of Physical Oceanography*, 41(6), 1160−1181. https://doi.org/10.1175/2011JPO4547.1

Farrar, J. T., Durland, T., Jayne, S. R., & Price, J. F. (2021). Long-distance radiation of Rossby waves from the equatorial current system. *Journal of Physical Oceanography*, 51(6), 1947−1966. https://doi.org/10.1175/JPO-D-20-0048.10

Gill, A. E. (1982). Atmosphere-ocean dynamics. *International Research Series.* (Vol. 30). San Diego, CA: Academic Press.

Hernández-Guerra, A., & Nykjaer, L. (1997). Sea surface temperature variability off north-west Africa: 1981–1989. *International journal of remote sensing*, 18(12), 2539–2558. https://doi.org/10.1080/014311697217468

Legeckis, R. (1977). Long waves in the eastern equatorial pacific ocean: a view from a geostationary satellite. *Science*, 197(4309), 1179−1181. https://science.sciencemag.org/content/197/4309/1179

Legeckis, R., Pichel, W., & Nesterczuk, G. (1983). Equatorial long waves in geostationary satellite observations and in a multichannel sea surface temperature analysis. *Bulletin of the American Meteorological Society*, 64(2), 133−139. https://doi.org/10.1175/1520-0477(1983)064<0133:ELWIGS>2.0.CO;2

Lyman, J. M., Johnson, G. C., & Kessler, W. S. (2007). Distinct 17- and 33-day tropical instability waves in subsurface observations. *Journal of Physical Oceanography*, 37(4), 855−872. https://doi.org/10.1175/JPO3023.1

Moum, J. N., Lien, R. C., Perlin, A., Nash, J. D., Gregg, M. C., & Wiles, P. J. (2009). Sea surface cooling at the equator by subsurface mixing in tropical instability waves. *Nature Geoscience*, 2(11), 761–765. https://doi.org/10.1038/ngeo657

Shinoda, T., Kiladis, G. N., & Roundy, P. E. (2009). Statistical representation of equatorial waves and tropical instability waves in the Pacific Ocean. *Atmospheric research*, 94(1), 37−44. https://doi.org/10.1016/j.atmosres.2008.06.002

Tanaka, Y., & Hibiya, T. (2019). Generation Mechanism of Tropical Instability Waves in the Equatorial Pacific Ocean. *Journal of Physical Oceanography*, 49(11), 2901−2915. https://doi.org/10.1175/JPO-D-19-0094.1

Tchilibou, M., Gourdeau, L., Morrow, R., Serazin, G., Djath, B., & Lyard, F. (2018). Spectral signatures of the tropical pacific dynamics from model and altimetry: A focus on the meso-submesoscale range. *Ocean Science*, 14(5), 1283−1301. https://doi.org/10.5194/os-14-1283-2018

Thomson, R. E., & Emery, W. J. (2014). Data analysis methods in physical oceanography, 3rd ed., New York: Elsevier.

Wang, C., & Fiedler, P. C. (2006). ENSO variability and the eastern tropical pacific: A review. *Progress in Oceanography*, 69(2-4), 239−266. https://doi.org/10.1016/j.pocean.2006.03.004

Warner, S. J., & Moum, J. N. (2019). Feedback of mixing to ENSO phase change. *Geophysical Research Letters*, 46(23), 13920–13927. https://doi.org/10.1029/2019GL085415

Willett, C. S., Leben, R. R., & Lavín, M. F. (2006). Eddies and tropical instability waves in the eastern tropical pacific: A review. *Progress in Oceanography*, 69(2-4), 218−238. https://doi.org/10.1016/j.pocean.2006.03.010